Chemical Engineering Journal 502 (2024) 157876

Contents lists available at ScienceDirect

Chemical Engineering Journal

journal homepage: www.elsevier.com/locate/cej

Visualization of strain rate based on mechanoluminescence tailing

Man Wang [a], Jianqiang Xiao [a], Jian Zhang [a], Lei Zhao [c], Yingdan Song [c], Zhichao Liu [a], Ting Wang [b], Xuhui Xu [a,*], Jie Yu [a,*]

[a] Faculty of Materials Science and Engineering, Yunnan Joint International Laboratory of Optoelectronic Materials and Devices, Kunming University of Science and Technology, Kunming 650093, PR China
[b] College of Materials and Chemistry & Chemical Engineering, Chengdu University of Technology, Chengdu 610059, PR China
[c] Baoji Key Laboratory of Micro-Nano Optoelectronics and Terahertz Technology, School of Physics and Opto-Electronic Technology, Collaborative Innovation Center of Rare-Earth Optical Functional Materials and Devices Development, Baoji University of Arts and Sciences, Baoji Shaanxi 721016, PR China

ARTICLE INFO

Keywords:
Mechanoluminescence
Mechanoluminescence lifetime
Rate sensing
Rate visualization

ABSTRACT

Mechanoluminescence (ML) materials have the ability to emit light under mechanical force, allowing for visible mechanical force distribution and making them valuable for applications in smart textiles and wearable sensors. Detecting the force rate is crucial for applications, such as haptic feedback devices and mechanical monitoring, but visualizing the speed of strain has not been achieved yet. In this study, we have successfully visualized the strain rate by monitoring the ML tailing lengths of red, green, and blue (RGB) ML materials, including CaF_2: Tm^{3+}, CaF_2: Eu^{3+}, and CaF_2: Tb^{3+} phosphors. These materials exhibit varying ML tailing lengths at identical rotation speed of friction force, due to their distinct lifetime of the emitting centers. By incorporating these RGB ML phosphors into a composite film, the discrepancies in ML tailing lengths across different colors become visible, with these differences becoming more pronounced as the rotation speeds rise. Ultimately, the visualization of rotational speed in bearings was achieved successfully based on the vivid color changes in the ML tailing length at different speeds.

1. Introduction

Force rate detection involves the comprehensive analysis and assessment of an object's motion characteristics by precisely measuring the intricate relationship between force and rate, and is widely utilized in various domains, including sports science [1,2], biomechanical research [3–5], material testing for strength [6] and durability [7], and meticulous mechanical safety monitoring [8–10]. Up to now, the force-rate data could be achieved by attaching the strain gauge to the surface of the object being measured, which are assisted by signal transmission and computer analysis. This method allows for the accurate measurement of forces acting on the object and the velocities at which it moves, providing valuable data for analysis and interpretation [11,12]. In addition, Digital Image Correlation (DIC) technology is also another commonly method to realize force-rate measurement, which involves high-speed camera to capture continuous images of a surface, and then analyze these images to track the displacement and deformation of the object [13–15]. However, the complexity of testing setups and high costs associated with equipment can limit the widespread application of these methods [16]. Therefore, there is a need for the development of more efficient and cost-effective measurement techniques in force-rate detection.

Recently, mechanoluminescence materials have emerged as a novel solution for converting mechanical stimuli into luminescent signals [17–20], enabling their application in wearable devices [21–23], structural stress monitoring [24–26], signal transmission [27–29], and dynamic stress imaging [30,31]. Integrating ML into force detection could potentially address the limitations of traditional measurement methods and enhance the efficiency and cost-effectiveness of the process [32,33]. Recently, researchers have made remarkable advancements in the ML functional applications. For instance, Soon Moon Jeong et al. ingeniously designed a wind-driven ML device to realize the colorful visualization of gas flow [34]. Rong-Jun Xie et al. innovatively realized the dual-mode visualization of stress and temperature distribution through based on the ML materials [35]. Besides, Yixi Zhuang et al. developed a close-range stress imaging device by combining ML film

* Corresponding authors at: Faculty of Materials Science and Engineering, Yunnan Joint International Laboratory of Optoelectronic Materials and Devices, Kunming University of Science and Technology, Kunming 650093, PR China (X. Xu).
E-mail addresses: xuxuh07@126.com (X. Xu), yujieone@163.com (J. Yu).

https://doi.org/10.1016/j.cej.2024.157876
Received 10 August 2024; Received in revised form 9 October 2024; Accepted 20 November 2024
Available online 23 November 2024

with CMOS technology, thus realizing the visualization of stress distribution [36]. While these studies have significantly progressed in ML functional applications and successfully visualized stress distribution [37–40], the visualization of the stress rate parameter remains an unexplored aspect in current research.

Generally, the duration of the ML signals emitted by ML materials can be changed by variation in the loading speed, which in turn affects the length of the ML tail. This is because rapid loading may not allow sufficient time for the molecular and crystalline structures of the material to rearrange and adapt during the deformation process, leading to stress concentration and energy accumulation, which results in a longer tail. Conversely, slow loading allows the material structure more time to adapt to stress changes, reducing the chances of stress concentration and resulting in a shorter tail. Therefore, it is predicted the variation in loading speed could be read out by monitoring the ML tail length. Hence, three types of ML materials, namely CaF_2: Eu^{3+}, CaF_2: Tb^{3+}, and CaF_2: Tm^{3+} phosphors, emitting red, green, and blue (RGB) light respectively, were constructed. These three ML phosphors exhibit varying ML tailing lengths at same loading speed, due to the distinct fluorescence lifetimes of the emitting centers. Consequently, the correlations between the lifetime of the emitting centers and the ML tailing lengths were meticulously investigated. By mixing these RGB ML phosphors into a composite film, the visualization of strain rate was carried out by observing the discrepancies in ML tailing lengths to the various emitting centers. Our findings demonstrate the potential application of the ML composite film in visually representing force rates in bearings through the vivid color changes in the ML tailing lengths.

2. Experiment section

2.1. Synthesis of ML powder

CaF_2: Tm^{3+}, CaF_2: Tb^{3+}, and CaF_2: Eu^{3+} phosphors were synthesized by using the high-temperature solid-state phase method. The raw materials include CaF_2 (99.9 %, Aladdi, Tb_4O_7(99.9 %, Aladdin), Tm_2O_3(99.9 %, Aladdin) and Eu_2O_3(99.9 %, Aladdin). First, the raw materials were precisely weighed based on the stoichiometric ratio and subsequently ground in an ethanol-containing agate mortar for 30 min until complete evaporation of the solvent. The resulting homogeneous mixture was then transferred into an alumina crucible, followed by sintering at 1000 °C for 2 h and cooling to room temperature. Finally, the sintered samples were ground to yield the ML material, ready for subsequent characterization.

2.2. Fabrication of CaF_2-Based ML composites

A uniform mixture was prepared by combining 1.5 g of ML powder with 2.5 g of polydimethylsiloxane (Sylgard 184 silicone elastomer, Dow Corning) at a precursor-to-curing agent weight ratio of 10:1. The homogeneous blend was subsequently poured into a circular mold (d = 4 cm) and cured at 80 °C for 2 h. The fabrication procedures for CaF_2: Tb^{3+} @ PU (polyurethane), CaF_2: Tb^{3+} @ SG (silica gel), and CaF_2: Tb^{3+} @ ER (epoxy resin) were analogous to those for CaF_2: Tb^{3+} @ PDMS (polydimethylsiloxane). All ML films synthesized by incorporating ML phosphors with PDMS in this study followed this preparation method (CaF_2: Tm^{3+} @ PDMS, CaF_2: Tb^{3+} @ PDMS, and CaF_2: Eu^{3+} @ PDMS). The weight ratios of base resin, curing agent, and CaF_2: Tb^{3+} were 2:2:1, 2:2:1, and 3:1:1 for CaF_2: Tb^{3+} @ PU, CaF_2: Tb^{3+} @ SG, and CaF_2: Tb^{3+} @ ER, respectively.

2.3. Material Characterizations

The crystal structure of the prepared powder was investigated via XRD (D8ADVANCE/Germany Bruker X-ray diffractometer) using a Cu–Kα radiation source (1.5418 Å, 40 kV, 30 mA). Surface topography and elemental mapping analyses of CaF_2: Tb^{3+} were performed by a scanning electron microscope (SEM, JIB-4700) PL, PL excitation, and PL decay curves were detected by a fluorescence spectrophotometer (FLS980, Edinburgh Instruments). The valence state of CaF_2:Tb^{3+} was confirmed via XPS (Thermo Fisher Scientific, ESCALAB 250Xi; energy scanning range of 0–5000 eV, resolution of 0.45 eV). The TL data was tested by a thermoluminescence meter (FJ-427A1) after irradiation under ultraviolet light for 15 min. SEL was generated by HC-BZ/F-120 kV high voltage electrostatic generator of Zhaoqing Hechuang Technology Co., Ltd. The CL spectrum was detected on the modified Mp-Micro-S instrument attached to the SEM. The triboelectric potential was measured using the electrostatic measuring probe (SK050, KEYENCE (Japan) Co., Ltd.) at a distance of 10 mm. We derived ML spectra form optical fibre spectrometer (QE65-pro, Ocean Optics) with multifunctional material surface property tester (MS-T3001) and get mechanics luminescence image by Nikon D7100 camera.

3. Results and Discussion

The XRD patterns of CaF_2: x%Tb^{3+} (x = 0.1, 0.2, 0.4, 0.6 and 0.8) are shown in Fig. 1**a**. The diffraction peaks align perfectly with the standard card (PDF#35–0816), and no extra impurity peaks are recorded, confirming the successful synthesis of the pure phase CaF_2 phosphor. Moreover, the XRD refinement of representative sample CaF_2: 0.4 % Tb^{3+} yielded fitting factors of Rwp = 9.8 %, Rp = 6.3 %, providing further evidence of the successful synthesis of the pure phase material (Fig. 1**b**). Fig. 1**c** reveals the crystal structure of CaF_2: Tb^{3+}. The CaF_2 possesses the typical fluorite structure with a face-centered cubic space group of Fm-3 m. In this structure, each Ca ion is coordinated to eight fluoride ions in a cubic arrangement, forming a [CaF8] hexahedron. Considering the atomic radius and coordination number, it is possible for Tb^{3+} (r = 1.04 Å, CN = 8) to replace the Ca^{2+} (r = 1.12 Å CN = 8) site in the CaF_2 structure. The scanning electron microscopy (SEM) and elements mapping of CaF_2: 0.4 %Tb^{3+} are given in **Fig. S1a**, which shows that the Ca, F and Tb elements are evenly distributed in CaF_2: 0.4 %Tb^{3+} particles. Furthermore, the additional XPS analysis of CaF_2: 0.4 %Tb^{3+} provides further confirmation the successfully introduction of Tb^{3+} in CaF_2 (Fig. 1**d**). The high-resolution XPS spectra of Tb 3d and Tb 4d, as shown in **Fig. S2**, confirm the successful incorporation of Tb^{3+} ions into the CaF_2 matrix.

To explore the ML performance of CaF_2: Tb^{3+}, the ML composited films are fabricated by mixing polydimethylsiloxane (PDMS) and the as-obtained phosphors. The as-obtained ML films manifest bright green light under various stress stimuli, such as rubbing, folding, stretching, and tearing (Fig. 2**a**), showcasing the ability to emit light in response to mechanical deformation. This green luminescence is consistent with the PL in **Fig. S3a**. With the increasing concentration of Tb^{3+}, the PL intensity increases initially and then decreases, the optimal doping concentration is 0.4 %. The optimal luminescence intensity and the appropriate doping concentration of rare earth ions were determined by the maximum intensity of the most prominent spectral band. The inset shows the PL digital picture of CaF_2: x%Tb^{3+} (x = 0.1, 0.2, 0.4, 0.6, 0.8), in which the CaF_2: 0.4 %Tb^{3+} possesses the strongest PL intensity (**Fig. S3b**). The ML spectra and the corresponding photographs of the CaF_2: Tb^{3+} composited films at varying Tb^{3+} concentration are given in Fig. 2**b**. These spectra reveal multiple emission peaks at 457 nm, 485 nm, 542 nm, 583 nm and 620 nm which are attributed to the characteristic emission $^5D_4$-^7F_i (i = 6,5,4,3) of Tb^{3+} ions. The ML intensity gradually increases and reaches its maximum when x = 0.4 %. The inset highlights that that the CaF_2: 0.4 %Tb^{3+} possesses the strongest ML intensity, consistent well with the recorded ML spectra. The centrosymmetric structure of CaF_2 makes it difficult to achieve the desired ideal-driven ML performance [41]. So, to investigate the ML mechanism of CaF_2: Tb^{3+}, the phenomenon and ML spectrum of CaF_2: Tb^{3+} powder embedded within polydimethylsiloxane (PDMS), epoxy resin (ER), polyurethane (PU), and silica gel (SG) are recorded under the same size of force in Fig. 2**c**. The results demonstrate that the ML performance is

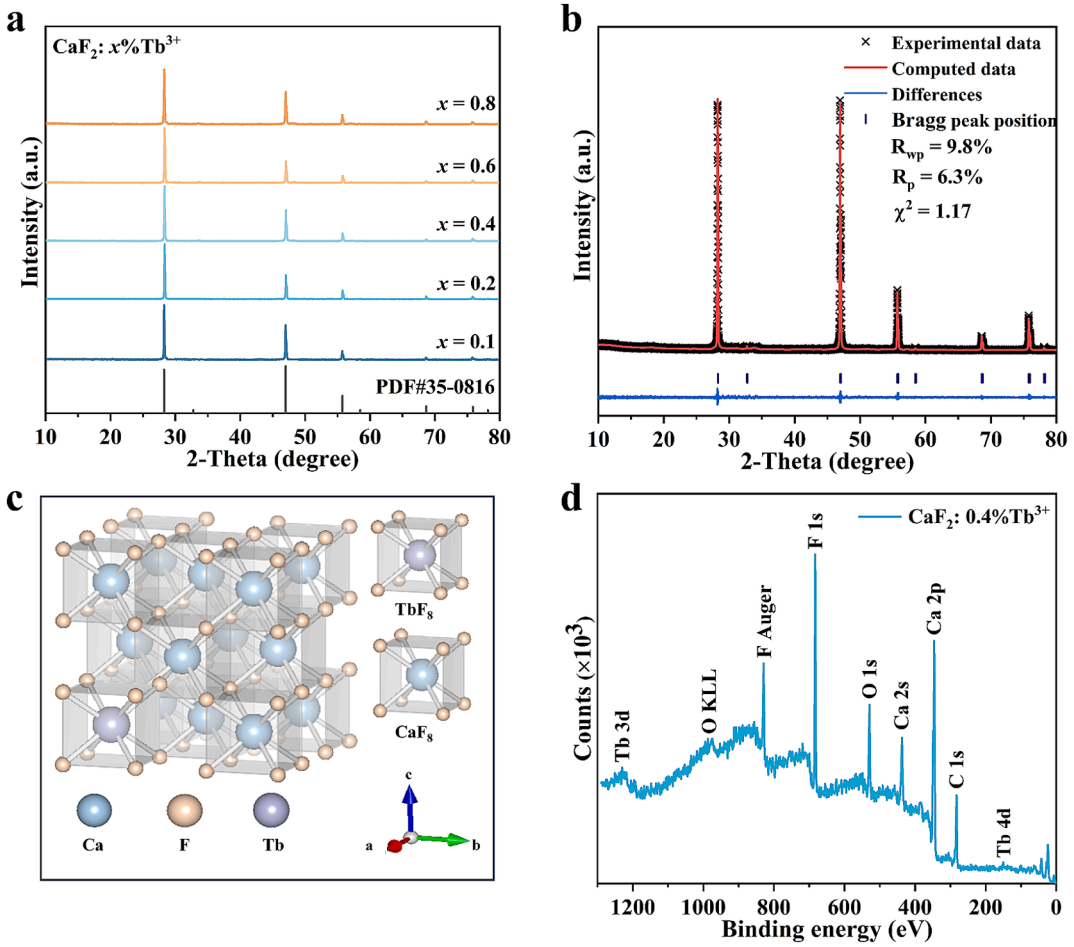

Fig. 1. (a) The XRD patterns of CaF_2: x%Tb^{3+} (x = 0.1, 0.2, 0.4, 0.6, and 0.8) phosphors. (b) The Rietveld refinement patterns of representative CaF_2: 0.4 %Tb^{3+} phosphor. (c) The crystal structure of the CaF_2: Tb^{3+}. (d) XPS survey curve of CaF_2: 0.4 %Tb^{3+} phosphor.

highly influenced by the polymer matrix. Among them, only CaF_2: Tb^{3+}@ PDMS and CaF_2: Tb^{3+}@ SG composites showcase obvious green ML behaviors. It is anticipated that the presence of specific polymer matrices together with the CaF_2: Tb^{3+} phosphors likely facilitate distinct interfacial phenomena that contribute to ML emission. Furthermore, the triboelectric potential measurements of CaF_2: Tb^{3+} phosphors and polymer matrix reveal that only PDMS and SG exhibit opposite the triboelectric potential to CaF_2: Tb^{3+}, inducing the triboelectricity phenomenon. This observation is in line with the ML behaviors depicted in Fig. 2**c**. As the same time, the **Fig. S4** shows there is no TL peak recorded after UV irradiation, which excluded the trap-controlled mechanoluminescence.

To further explore the triboelectric ML furtherly, the CL, SEL and ML spectra of CaF_2: Tb^{3+} were recorded. It is observed that the ML spectrum exhibits the same profile to SEL spectrum rather that CL spectrum (Fig. 2**e**). The spectrum of CL is identified as $^5D_3$-^7F_j transition, which is different from the $^5D_4$-^7F_j transition of SEL and ML [41]. This observation supports the conclusion that mechanoluminescence is not triggered by electron bombardment, providing solid evidence that its luminescence mechanism is induced by triboelectricity. We further tested the CL spectra at different concentrations and different voltages, and the results showed only the change of CL intensity rather than the peak position (**Fig. S8**). Additionally, the friction potential values of CaF_2: Tb^{3+} @ PDMS under different forces are displayed in Fig. 2**f**, which evident that the intensity of friction potential gradually rise with increasing force. The friction potential strength of CaF_2: Tb^{3+} @ PDMS depends on the applied force, which supports the view that the ML behavior is closely related to the constructed friction potential difference. Moreover, Fig. 2**g** presents the photoluminescence spectra of CaF_2: Tb^{3+} as a function of voltage. The electrostatic luminescence intensity exhibits a linear growth pattern with increasing voltage. It is worth noting that by adjusting the excitation voltage of the SEL device, the difference in the friction potential can be effectively simulated, so that the relationship between the friction potential and the resulting ML intensity can be studied, which further confirms the force-friction potential-induced ML process. Then, we characterized the ML intensity of CaF_2: Tb^{3+} @ PDMS under different forces (Fig. 2**h**), demonstrating a linear relationship between ML intensity and force.

Accordingly, ML mechanism of CaF_2: Tb^{3+}@PDMS can be elucidated as follows (Fig. 2**i**): i) Initially, the electron clouds of surface atoms of CaF_2: Tb^{3+} particles and PDMS polymer remain non-overlapping, existing as two distinct potential wells. ii) Upon compounding, the CaF_2: Tb^{3+} particles and PDMS polymer come into full contact within the elastomers, leading to the overlap of their electron clouds and the establishment of a covalent bond. iii) The overlapping of the individual potential wells facilitates electron transfer from the CaF_2: Tb^{3+} particles to the PDMS polymer due to a decrease in the energy barrier. iv) When the CaF_2: Tb^{3+} @PDMS elastomer film is subjected to friction, the extent of electron cloud overlap alters. Consequently, electrons swiftly transfer back to the holes, instigating ML behavior through the ensuing electron-hole recombination process [42].

Additionally, we have developed RGB ML materials, including CaF_2: Tm^{3+} and CaF_2: Eu^{3+}, as well as CaF_2: Tb^{3+} (**Fig. S1**). We measured the ML spectra of CaF_2: Tm^{3+} and CaF_2: Eu^{3+} at different concentrations, and selected the best concentration for subsequent research (**Fig. S5**). The emission peaks at 457, 482, 505,681 and 800 nm in **Fig. S5a** belong

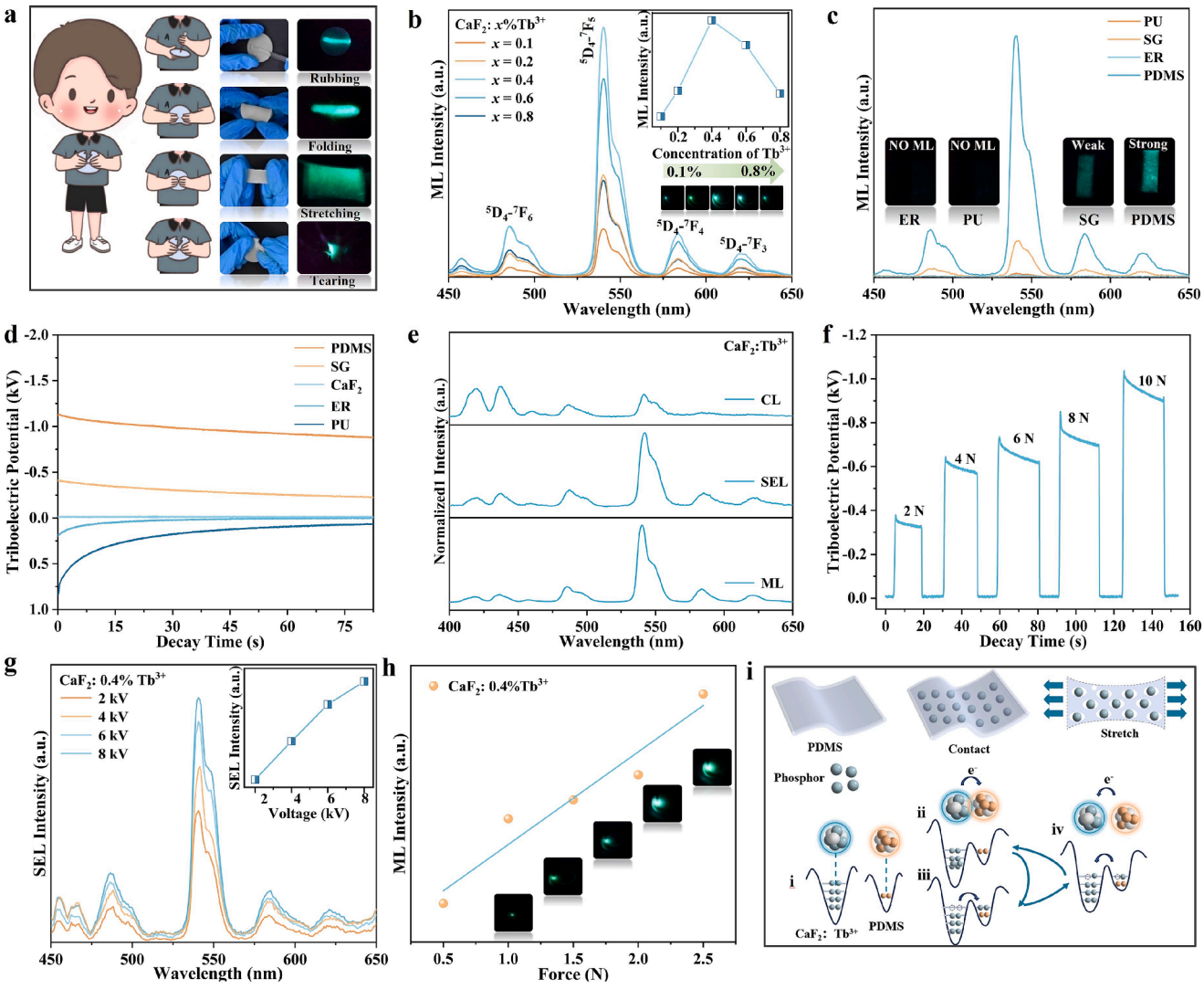

Fig. 2. (a) The ML photographs of the CaF_2: Tb^{3+} composited film under the mechanical stimuli of rubbing, folding, stretching, and tearing. (b) The ML spectra and corresponding photographs of CaF_2: $x\%Tb^{3+}$ (x = 0.1 %, 0.2 %, 0.4 %, 0.6 %, and 0.8 %) under 2 N stress, the inset shows the ML intensity as a function of Tb^{3+} concentration. (c) Physical photos and ML spectra of CaF_2: Tb^{3+} @ PDMS, CaF_2: Tb^{3+} @SG, CaF_2: Tb^{3+} @ER, and CaF_2: Tb^{3+} @PU) under stretching. (d) Friction potential of CaF_2: Tb^{3+} powder and CaF_2: Tb^{3+} @ PDMS, CaF_2: Tb^{3+} @SG, CaF_2: Tb^{3+} @ER, and CaF_2: Tb^{3+} @PU. (e) CL, SEL, and ML spectra of CaF_2: 0.4 $\%Tb^{3+}$. (f) Friction potential attenuation regulation of CaF_2: Tb^{3+}@PDMS under different stress. (g) SEL spectra of CaF_2: 0.4 % Tb^{3+} as a function of voltage. (h) ML intensity variations and physical photos of CaF_2: Tb^{3+} @ PDMS under different stress. (i) ML mechanism of CaF_2: Tb^{3+}.

to the $^1D_2$-$^3F_4$, $^1G_4$-$^3H_6$, $^1D_2$-$^3H_5$, $^3F_3$-$^3H_6$ and $^3H_4$-$^3H_6$ transition of Tm^{3+}, respectively and the emission peaks at 317, 236, 608, 624, 655 and 709 nm in **Fig. S5b** belong to the $^5D_0 \rightarrow {}^7F_J$ (J = 0,1,2,3,4) transition of Eu^{3+}, respectively. Fig. 3**a** illustrates that the composites of CaF_2: Tm^{3+}, CaF_2: Eu^{3+}, CaF_2: Tb^{3+} exhibit bright RGB ML emissions, and the ML tailing length gradually increases with the increase of the rotational speed (Fig. 3**b**). Moreover, CaF_2: Tb^{3+} composite shows longest ML tail compared with other two doped ion composites, which is may attributed to the longer lifetime of Tb^{3+}. When the lifetime of the emission centers is shorter, they transition back to the ground state more quickly, resulting in a shorter fluorescence duration and tail length. Conversely, when the fluorescence lifetime of the emission centers is longer, they stay in the excited state for a longer time, leading to a longer duration of luminescence events and consequently a longer tail. To demonstrate this proposed the observed distinct ML tail, the luminescence lifetime of CaF_2: Tm^{3+} is 1.9 μs, CaF_2: Eu^{3+} is 1.337 ms and CaF_2: Tb^{3+} is 2.6 ms by fitting calculation (Fig. 3**b**). Thus, it can be inferred that emission centers with longer fluorescence lifetimes tend to exhibit longer fluorescence tails (Fig. 3**c**). **Fig. S9 and** Fig. 3**d** are lifetime decay curves of the CaF_2: 0.15 $\%Tm^{3+}$, CaF_2: 5.0 $\%Eu^{3+}$ and CaF_2: 0.4 $\%Tb^{3+}$ at 298, 323 and 348 K, respectively. The lifetime of three composites were subjectively decreased by increasing the operation temperature. Subsequently, the ML tailing length at different temperatures are recorded in Fig. 3**e**, we extracted the ML tailing lengths of CaF_2: Tm^{3+}, CaF_2: Eu^{3+} and CaF_2: Tb^{3+} at different temperatures as shown in Fig. 3**f**, which manifests that the ML tailing length decreases as the temperature increases, thereby confirming the earlier hypothesis. However, the ML tailing length remains constant with the increase in force, with only the luminescence intensity increasing. The spectrum of the change of the intensity of mechanical luminescence with the magnitude of the force is shown in **Fig. S6** and Fig. 2**b**. This confirms that the ML tailing length is independent of the applied force (**Fig. S7**). Therefore, rotational speed can be visually detected by recording the ML tailing length at different emission colors.

The observation of a difference in ML tailing lengths at the same rotation speed is attributed to the diverse fluorescence lifetimes of various emission centers. Consequently, combining these RGB ML phosphors into a composite film can effectively be used for visually detecting rotation speeds through the gap in ML tailing lengths. As depicted in Fig. 4**a**, the fabrication of the composite film involves

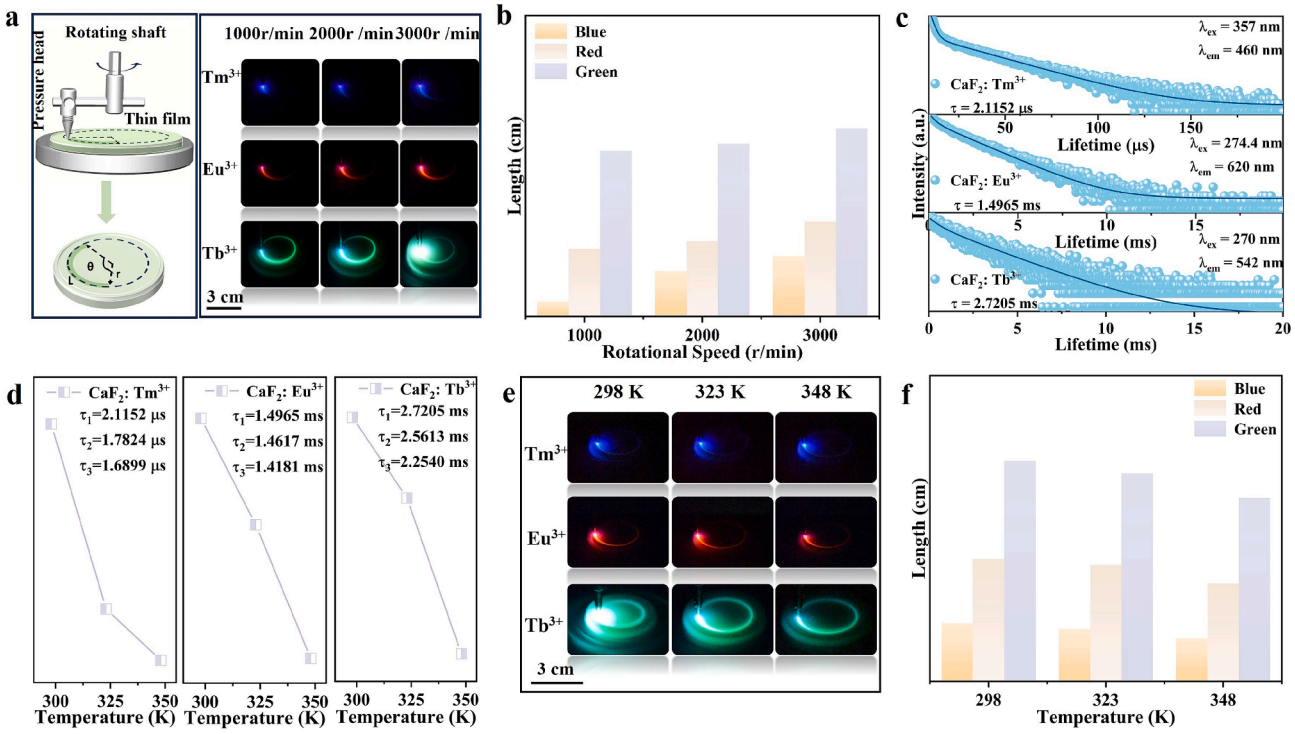

Fig. 3. (a) The ML photographs of CaF_2: 0.15 %Tm^{3+}@ PDMS, CaF_2: 5.0 %Eu^{3+}@ PDMS and CaF_2: 0.4 %Tb^{3+}@ PDMS at distinct rotational speed (1000, 2000 and 3000 r/min). (b) The relationship between the ML trailing length and the rotational speed. (c) Lifetime decay curves of the CaF_2: 0.15 %Tm^{3+}, CaF_2: 5.0 %Eu^{3+} and CaF_2: 0.4 %Tb^{3+}. (d) the calculated lifetime value and (e) ML photographs of CaF_2: 0.15 %Tm^{3+}, CaF_2: 5.0 %Eu^{3+} and CaF_2: 0.4 %Tb^{3+} at distinct operation temperature (298, 323 and 348 K). (f) The relationship between the ML trailing length and operation temperature.

physically mixing multi-colored ML phosphors with PDMS. Fig. 4**b** displays physical photos of the CaF_2: 5.0 %Eu^{3+}&CaF_2: 0.4 %Tb^{3+} composite film at various mixing ratios under different rotational speeds. By altering the mixing ratio of CaF_2: 5.0 %Eu^{3+} and CaF_2: 0.4 %Tb^{3+}, the color of the mechanics luminescence tailing demonstrates a distinct variation. Furthermore, with the increase in rotation speed, the ML tailing length gradually extends, demonstrating its potential for visual rotation speed detection. Not only that, the physical photos of CaF_2: 0.15 % Tm^{3+} and CaF_2: 0.4 % Tb^{3+}, CaF_2: 0.15 % Tm^{3+} and CaF_2: 5.0 % Eu^{3+} at different speeds also have the same law (**Fig. S10**). Specifically, when CaF_2: 5.0 %Eu^{3+} and CaF_2: 0.4 %Tb^{3+} are mixed in a 6:4 ratio, noticeable differences in tailing length and color variations can be observed. Consequently, we selected this ratio for conducting a thorough investigation of the composite film. In Fig. 4**c**, separated red and green ML tailing length are presented, derived from the recorded ML image. The red and green ML tailing lengths are detailed in Fig. 4**d**, demonstrating a gradual extension as the rotation speed increases. Importantly, there is a notable difference in the rate of extension between the red and green tails, leading to a conspicuous gap in ML tailing lengths. Accordingly, the discrepancy in ML tailing lengths between red and green is summarized in Fig. 4**e**. As the rotation speed increases, the discrepancy becomes more pronounced, thereby enhancing the possibility of visually detecting the rotation speed. Furthermore, to enhance the color variations, CaF_2: Tm^{3+}, CaF_2: Eu^{3+}, and CaF_2: Tb^{3+} were mechanically blended at a ratio of 3:2:1 with PDMS to produce an RGB composite ML film. In Fig. 4**f**, the RBG composite ML film exhibits a multi-color ML tailing gap with the escalating rotation speed of the friction machine. Within the increase of rotational speed, the ML tailing gaps with red and green colors are significantly apparent, expanding the color wavelength range and facilitating visual detection. Subsequently, the original image was color-separated into blue, red, and green hues, represented in ii, iii, and iv in Fig. 4**f**. It is observable that with the increase in rotation speed, the tailing lengths of each color more prominent. The alterations in the quantified tailing lengths are depicted in Fig. 4**g**. With the increase of rotational speed, not only the ML tailing length increases, but also the tailing difference of the three colors gradually grows. The vivid color changes in the trailing colors at different speeds offer us a novel and innovative strategy to visually represent the rotational speed.

By detecting the differences of the tailing length of multicolor ML film, a visual detection of rotational speed can be achieved. Therefore, we propose to utilize the developed ML multicolor film for detecting the rotational speed of bearings. In this study, ML multicolor composite films, CaF_2:Tm^{3+}, CaF_2:Eu^{3+}, CaF_2:Tb^{3+} @ PDMS, were fabricated and then attached to the inner wall of acrylic tubes. The internal structure of the bearing was simulated using MS-T3001, as shown in Fig. 5**a**, to measure the rotational speed of the bearing by minoring the ML tailing colors on the surface of the composite film. We use the camera to record the real test process in the support video, and we can clearly see the process of tailing length change. The detailed tailing length can be obtained by frame-by-frame analysis. Detailed tailings length can be obtained by frame-by-frame analysis. Under different loading rates, ML tailing photos of the composite film were recorded using a camera (Fig. 5**b**). Subsequently, Adobe Photoshop 2020 software was employed to separate the hue of the original images, extracting the blue, red, and green ML tailing lengths individually as shown in ii, iii, and iv of Fig. 5**b**. Detailed length values are provided in Fig. 5**c**. Therefore, by calculating the differences between them, we achieved a visual detection of rotational speed. This method provides a new innovative way for rate visualization, reflecting the changes in rotation speed through color variation, offering a clearer description for mechanical structure detection and quantitative analysis.

4. Conclusion

In conclusion, force-friction potential-induced RGB ML materials, including CaF_2: Tm^{3+}, CaF_2: Eu^{3+}, and CaF_2: Tb^{3+} phosphors, were synthesized. The study revealed that an increase in rotational speed led

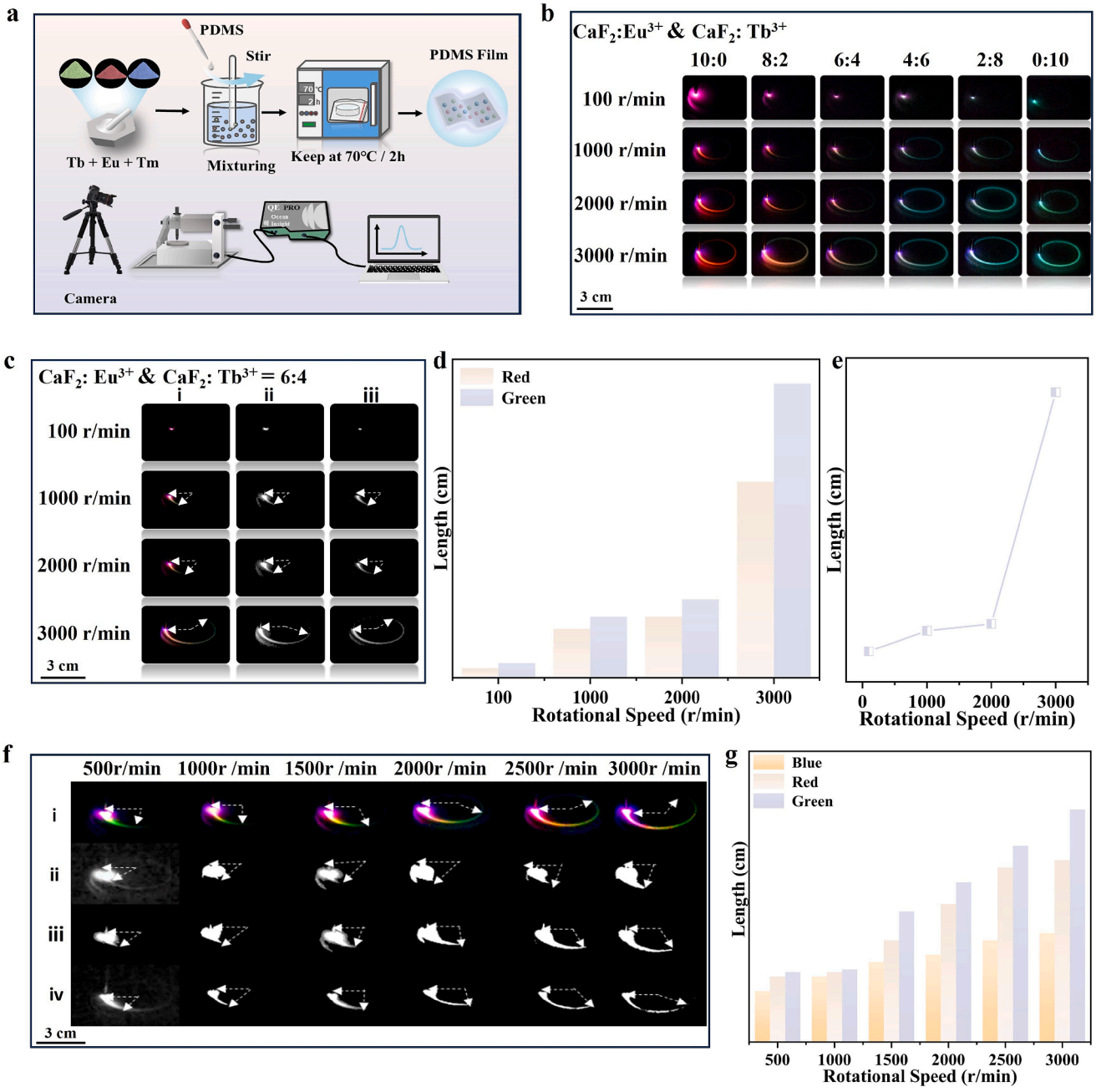

Fig. 4. (a) Schematic illustration of the preparation process for the multi-color ML film and the corresponding setup for the rotating friction experiment. (b) Physical photos of the CaF_2: 5.0 %Eu^{3+}&CaF_2: 0.4 %Tb^{3+} composited film at various mixing ratios under different rotational speeds. (c) Photos of the CaF_2: 5.0 %Eu^{3+} and CaF_2: 0.4 %Tb^{3+} composite PDMS film with a ratio of 6:4, including (i) ML color images (ii) and separated red (iii) and green ML images. (d) Relationship between the red and green ML tailing lengths of the composite film and rotational speeds of RG composite film. (e) Difference in ML tailing lengths between red and green. (f) Physical photos of the CaF_2: 0.15 %Tm^{3+}, CaF_2: 5.0 %Eu^{3+}, and CaF_2: 0.4 %Tb^{3+} composited films at different rotational speeds, (i) ML color images (ii) and separated blue (iii), red (iv) and green ML images. (g) Relationship between the RGB ML tailing lengths and rotational speeds of RGB composited film. (For interpretation of the references to color in this figure legend, the reader is referred to the web version of this article.)

to longer ML tailing lengths in the same ML film, indicating the successful readout of stress rate through monitoring these changes. Furthermore, the distinct fluorescence lifetimes of the emitting centers resulted in varying ML tailing lengths at identical loading speeds. Accordingly, by incorporating these RGB ML phosphors into a flexible film, the observation of the gap in ML tailing lengths among different colors at the same rotation speed can be visible, with the gap becoming more pronounced as the strain rate increases. Finally, we demonstrated that this technology allows for the visual detection of stress rates in bearings through the length and color changes in ML tailing.

CRediT authorship contribution statement

Man Wang: Writing – review & editing, Writing – original draft, Investigation, Formal analysis, Data curation, Conceptualization. **Jianqiang Xiao:** Software, Methodology. **Jian Zhang:** Investigation, Data curation. **Lei Zhao:** Supervision, Resources. **Yingdan Song:** Data curation. **Zhichao Liu:** Visualization. **Ting Wang:** Writing – review & editing, Formal analysis. **Xuhui Xu:** Supervision, Resources, Project administration. **Jie Yu:** Visualization, Supervision, Resources.

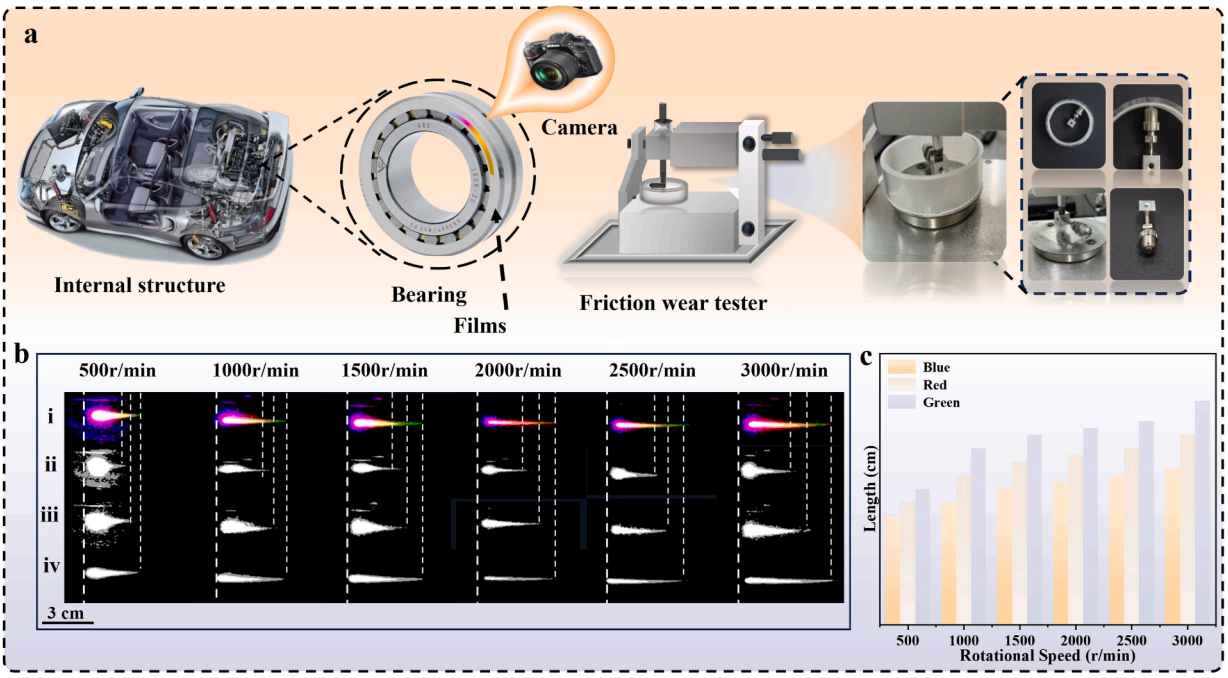

Fig. 5. (a) Visual detection of rotational speed in bearings based on RGB ML film. (b) Photographs of the ML image of RGB ML film, and RGB separated images after hue extraction. (c) Quantitative analysis data of the ML tailing varying with rotational speed.

Declaration of competing interest

The authors declare that they have no known competing financial interests or personal relationships that could have appeared to influence the work reported in this paper.

Acknowledgment

This work was financially supported by the National Natural Science Foundation of China (12364044), Yunnan Major Scientific and Technological Projects (202302AQ370003, 202402AB080011), Special Science and Technology Research Project of Yunnan Province for the South Asia and Southeast Asia Innovation Center (202403AP140006), the International Joint Innovation Platform of Yunnan Province (202203AP140004), the Outstanding Youth Project of Yunnan Province Applied Basic Research Project (202401AV070012),Natural Science Foundation of Shaanxi Province of China (NO. 2024JC-YBMS-042).

Appendix A. Supplementary data

Supplementary data to this article can be found online at https://doi.org/10.1016/j.cej.2024.157876.

Data availability

Data will be made available on request.

References

[1] J. Chen, Z. Zhou, B.J. Kim, Y. Zhou, Z. Wang, T. Wan, J. Yan, J. Kang, J.-H. Ahn, Y. Chai, Optoelectronic graded neurons for bioinspired in-sensor motion perception, Nat. Nanotechnol. 18 (8) (2023) 882–888, https://doi.org/10.1038/s41565-023-01379-2.

[2] C.S. Boland, U. Khan, C. Backes, A. O'Neill, J. McCauley, S. Duane, R. Shanker, Y. Liu, I. Jurewicz, A.B. Dalton, J.N. Coleman, Sensitive, High-Strain, High-Rate Bodily Motion Sensors Based on Graphene Rubber Composites, ACS Nano 8 (2014) 8819–8830.

[3] S. Shin, K. Baek, Y. Choi, H. So, Utilization of Machine Learning Techniques in Hot-Film Based Airflow Rate Sensors for Improving Flow Measurement, Adv. Intell. Syst. (2024) 2300711, https://doi.org/10.1002/aisy.202300711.

[4] E.A. Zimmermann, B. Gludovatz, E. Schaible, B. Busse, R.O. Ritchie, Fracture resistance of human cortical bone across multiple length-scales at physiological strain rates, Biomaterials 35 (21) (2014) 5472–5481, https://doi.org/10.1016/j.biomaterials.2014.03.066.

[5] G.F. Tyers, Current Status of Sensor-Modulated Rate-Adaptive Cardiac Pacing, J. Am. Coll. Cardiol. 15 (1990) 412.

[6] C. Buzea, K. Robbie, State of the art in thin film thickness and deposition rate monitoring sensors, Rep. Prog. Phys. 68 (2) (2005) 385–409, https://doi.org/10.1088/0034-4885/68/2/r04.

[7] H.F. Li, P. Zhang, B. Wang, Z.F. Zhang, Predictive fatigue crack growth law of high-strength steels, J. Mater. Sci. Technol. 100 (2022) 46–50, https://doi.org/10.1016/j.jmst.2021.04.042.

[8] H. Wang, S. To, C.Y. Chan, C.F. Cheung, W.B. Lee, Dynamic modelling of shear band formation and tool-tip vibration in ultra-precision diamond turning, Int. J. Mach. Tools Manuf. 51 (6) (2011) 512–519, https://doi.org/10.1016/j.ijmachtools.2011.02.010.

[9] L. Zhou, Y. Wang, Z. Ge, Z. Song, Multirate Factor Analysis Models for Fault Detection in Multirate Processes, IEEE Trans. Ind. Inform. 15 (7) (2019) 4076–4085, https://doi.org/10.1109/tii.2018.2889750.

[10] X. Hao, W. Du, Y. Zhao, Z. Sun, Q. Zhang, S. Wang, H. Qiao, Dynamic tensile behaviour and crack propagation of coal under coupled static-dynamic loading, Int. J. Min. Sci. Technol. 30 (5) (2020) 659–668, https://doi.org/10.1016/j.ijmst.2020.06.007.

[11] X. Ye, B. Shi, M. Li, Q. Fan, X. Qi, X. Liu, S. Zhao, L. Jiang, X. Zhang, K. Fu, L. Qu, M. Tian, All-textile sensors for boxing punch force and velocity detection, Nano Energy 97 (2022) 107114, https://doi.org/10.1016/j.nanoen.2022.107114.

[12] Z. Zhang, S. Wang, C. Liu, R. Xie, W. Hu, P. Zhou, All-in-one two-dimensional retinomorphic hardware device for motion detection and recognition, Nat. Nanotechnol. 17 (1) (2021) 27–32, https://doi.org/10.1038/s41565-021-01003-1.

[13] H.G. Shin, S. Timilsina, K.S. Sohn, J.S. Kim, Digital Image Correlation Compatible Mechanoluminescent Skin for Structural Health Monitoring, Adv. Sci. 9 (11) (2022) 2105889, https://doi.org/10.1002/advs.202105889.

[14] N.A. Hoult, M. Dutton, A. Hoag, W.A. Take, Measuring Crack Movement in Reinforced Concrete Using Digital Image Correlation: Overview and Application to Shear Slip Measurements, Proc. IEEE 104 (8) (2016) 1561–1574, https://doi.org/10.1109/jproc.2016.2535157.

[15] N. McCormick, J. Lord, Digital Image Correlation, Mater. Today 13 (12) (2010) 52–54, https://doi.org/10.1016/s1369-7021(10)70235-2.

[16] M. Ozon, A. Frasie, G. Gagnon-Turcotte, M. Roudjane, L. Bouyer, G. Gagnon, Y. Messaddeq, B. Gosselin, Motion Detection and Analysis Using Multimaterial Fiber Sensors, IEEE Trans. Circuits Syst. I-Regul. Pap. 70 (9) (2023) 3522–3533, https://doi.org/10.1109/tcsi.2023.3293000.

[17] N.C. Eddingsaas, K.S. Suslick, Light from sonication of crystal slurries, Nature 444 (7116) (2006) 163, https://doi.org/10.1038/444163a.

[18] H. Yang, Y. Wei, H. Ju, X. Huang, J. Li, W. Wang, D. Peng, D. Tu, G. Li, Microstrain-Stimulated Elastico-Mechanoluminescence with Dual-Mode Stress Sensing, Adv. Mater. (2024) 2401296, https://doi.org/10.1002/adma.202401296.

[19] B. Chen, X. Zhang, F. Wang, Expanding the Toolbox of Inorganic Mechanoluminescence Materials, Accounts Mater. Res. 2 (5) (2021) 364–373, https://doi.org/10.1021/accountsmr.1c00041.
[20] H. Terada, H. Imai, Y. Oaki, Visualization and Quantitative Detection of Friction Force by Self-Organized Organic Layered Composites, Adv. Mater. 30 (27) (2018) 1801121, https://doi.org/10.1002/adma.201801121.
[21] N. Li, S. Yu, L. Zhao, P. Zhang, Z. Wang, Z. Wei, W. Chen, X. Xu, Recoverable Dual-Modal Responsive Sensing Materials Based on Mechanoluminescence and Thermally Stimulated Luminescence toward Noncontact Tactile Sensors, Inorg. Chem. 62 (5) (2023) 2024–2032, https://doi.org/10.1021/acs.inorgchem.2c03540.
[22] S.J. Kim, F. Yang, H.S. Jung, G. Hong, S.K. Hahn, Mechanoluminescence and Mechanical Quenching of Afterglow Luminescent Particles for Wearable Photonic Display, Adv. Funct. Mater. (2024) 2314861, https://doi.org/10.1002/adfm.202314861.
[23] X. Qian, Z. Cai, M. Su, F. Li, W. Fang, Y. Li, X. Zhou, Q. Li, X. Feng, W. Li, X. Hu, X. Wang, C. Pan, Y. Song, Printable Skin-Driven Mechanoluminescence Devices via Nanodoped Matrix Modification, Adv. Mater. 30 (25) (2018) 1800291, https://doi.org/10.1002/adma.201800291.
[24] B. Tian, Z. Wang, A.T. Smith, Y. Bai, J. Li, N. Zhang, Z. Xue, L. Sun, Stress-induced color manipulation of mechanoluminescent elastomer for visualized mechanics sensing, Nano Energy 83 (2021) 105860, https://doi.org/10.1016/j.nanoen.2021.105860.
[25] J. Xiao, Y. Cai, Y. Song, H. Tang, P. Zhang, Q. Peng, X. Xu, Z. Liu, L. Zhao, High Stable Mechanoluminescence from $TbBO_3$ GCs for Stress Safety Monitoring, Laser Photon. Rev. 18 (3) (2023) 2301002, https://doi.org/10.1002/lpor.202301002.
[26] Y. Cai, S. Liu, L. Zhao, C. Wang, H. Lv, B. Liu, J. Qiu, X. Xu, X. Yu, Delayed stress memory by $CaAl_2O_4:Eu^{2+}$ mechanoluminescent phosphor with defect engineering regulation, J. Adv. Ceram. 11 (8) (2022) 1319–1329, https://doi.org/10.1007/s40145-022-0614-2.
[27] L. Li, C. Cai, X. Lv, X. Shi, D. Peng, J. Qiu, Y. Yang, Stress-Triggered Mechanoluminescence in ZnO-Based Heterojunction for Flexible and Stretchable Mechano-Optics, Adv. Funct. Mater. 33 (32) (2023) 2301372, https://doi.org/10.1002/adfm.202301372.
[28] H. Liang, Y. He, M. Chen, L. Jiang, Z. Zhang, X. Heng, L. Yang, Y. Hao, X. Wei, J. Gan, Z. Yang, Self-Powered Stretchable Mechanoluminescent Optical Fiber Strain Sensor, Adv. Intell. Syst. 3 (9) (2021) 2100035, https://doi.org/10.1002/aisy.202100035.
[29] X. Yang, Y. Cheng, Z. Liu, J. Zhang, J. Xu, H. Lin, Y. Wang, Designing Ratiometric Mechanoluminescence via Threshold Manipulation in Sandwich Structures, Laser Photon. Rev. 18 (3) (2023) 2301004, https://doi.org/10.1002/lpor.202301004.
[30] J.C. Zhang, C. Pan, Y.F. Zhu, L.Z. Zhao, H.W. He, X. Liu, J. Qiu, Achieving Thermo-Mechano-Opto-Responsive Bitemporal Colorful Luminescence via Multiplexing of Dual Lanthanides in Piezoelectric Particles and its Multidimensional Anticounterfeiting, Adv. Mater. 30 (49) (2018) 1804644, https://doi.org/10.1002/adma.201804644.
[31] P. Zhang, Z. Teng, L. Zhao, Z. Liu, X. Yu, X. Zhu, S. Peng, T. Wang, J. Qiu, Q. Wang, X. Xu, Multi-Dimensional Mechanical Mapping Sensor Based on Flexoelectric-Like and Optical Signals, Adv. Sci. 10 (19) (2023) 2301214, https://doi.org/10.1002/advs.202301214.
[32] C. Chen, Z. Lin, H. Huang, X. Pan, T.L. Zhou, H. Luo, L. Jin, D. Peng, J. Xu, Y. Zhuang, R.J. Xie, Revealing the Intrinsic Decay of Mechanoluminescence for Achieving Ultrafast-Response Stress Sensing, Adv. Funct. Mater. 33 (46) (2023) 2304917, https://doi.org/10.1002/adfm.202304917.
[33] Z. Qiu, W. Zhao, M. Cao, Y. Wang, J.W.Y. Lam, Z. Zhang, X. Chen, B.Z. Tang, Dynamic Visualization of Stress/Strain Distribution and Fatigue Crack Propagation by an Organic Mechanoresponsive AIE Luminogen, Adv. Mater. 30 (44) (2018) 1803924, https://doi.org/10.1002/adma.201803924.
[34] S.M. Jeong, S. Song, K.-I. Joo, J. Kim, S.-H. Hwang, J. Jeong, H. Kim, Bright, wind-driven white mechanoluminescence from zinc sulphide microparticles embedded in a polydimethylsiloxane elastomer, Energy Environ. Sci. 7 (10) (2014) 3338–3346, https://doi.org/10.1039/c4ee01776e.
[35] C. Chen, Y. Zhuang, X. Li, F. Lin, D. Peng, D. Tu, A. Xie, R.J. Xie, Achieving Remote Stress and Temperature Dual-Modal Imaging by Double-Lanthanide-Activated Mechanoluminescent Materials, Adv. Funct. Mater. 31 (25) (2021) 2101567, https://doi.org/10.1002/adfm.202101567.
[36] Y. Zhuang, X. Li, F. Lin, C. Chen, Z. Wu, H. Luo, L. Jin, R.J. Xie, Visualizing Dynamic Mechanical Actions with High Sensitivity and High Resolution by Near-Distance Mechanoluminescence Imaging, Adv. Mater. 34 (36) (2022) 2202864, https://doi.org/10.1002/adma.202202864.
[37] J. Ning, Y. Zheng, Y. Ren, L. Li, X. Shi, D. Peng, Y. Yang, MgF2:Mn2+: novel material with mechanically-induced luminescence, Sci. Bull. 67 (7) (2022) 707–715, https://doi.org/10.1016/j.scib.2021.12.005.
[38] X. Zheng, Y. Cheng, Y. Gao, T. Hu, J. Xu, H. Lin, Y. Wang, Doping dependent dual-response mechanoluminescence in $ZnGa_2O_4$, J. Mater. Chem. C 11 (5) (2023) 1747–1753, https://doi.org/10.1039/d2tc05086b.
[39] Y. Fujio, C.-N. Xu, Y. Terasawa, Y. Sakata, J. Yamabe, N. Ueno, N. Terasaki, A. Yoshida, S. Watanabe, Y. Murakami, Sheet sensor using SrAl2O4:Eu mechanoluminescent material for visualizing inner crack of high-pressure hydrogen vessel, Int. J. Hydrog. Energy 41 (2) (2016) 1333–1340, https://doi.org/10.1016/j.ijhydene.2015.10.073.
[40] X. Wang, H. Zhang, R. Yu, L. Dong, D. Peng, A. Zhang, Y. Zhang, H. Liu, C. Pan, Z. L. Wang, Dynamic Pressure Mapping of Personalized Handwriting by a Flexible Sensor Matrix Based on the Mechanoluminescence Process, Adv. Mater. 27 (14) (2015) 2324–2331, https://doi.org/10.1002/adma.201405826.
[41] W. Wang, S. Wang, Y. Gu, J. Zhou, J. Zhang, Contact-separation-induced self-recoverable mechanoluminescence of $CaF_2:Tb^{3+}$/PDMS elastomer, Nat. Commun. 15 (1) (2024) 2014, https://doi.org/10.1038/s41467-024-46432-3.
[42] Z.L. Wang, A.C. Wang, On the origin of contact-electrification, Mater. Today 30 (2019) 34–51, https://doi.org/10.1016/j.mattod.2019.05.016.